International Journal of Heat and Fluid Flow 29 (2008) 612–625

Contents lists available at ScienceDirect

International Journal of Heat and Fluid Flow

journal homepage: www.elsevier.com/locate/ijhff

Direct numerical simulation of a separation bubble on a rounded finite-width leading edge

Eric Lamballais [a,*], Jorge Silvestrini [b], Sylvain Laizet [a,c]

[a] *Laboratoire d'Etudes Aérodynamiques UMR 6609, Université de Poitiers, ENSMA, CNRS, Téléport 2 – Bd. Marie et Pierre Curie B.P. 30179, 86962 Futuroscope Chasseneuil Cedex, France*

[b] *Faculdade de Engenharia, Pontifícia Universidade Católica do Rio Grande do Sul, Av. Ipiranga 6681, 90619-900 Porto Alegre – RS, Brazil*

[c] *Department of Aeronautics, Imperial College London, South Kensington Campus, London SW7 2AZ, UK*

ARTICLE INFO

Article history:
Received 9 November 2007
Received in revised form 29 February 2008
Accepted 8 March 2008
Available online 13 May 2008

Keywords:
Separation bubble
Vortex dynamics
Convective/absolute stability
Direct numerical simulation
Immersed boundary method

ABSTRACT

The formation of a separation bubble over a generic half-body with a rounded edge is studied by direct numerical simulation. A single Reynolds number $Re = 1250$ (based on the body height H_s and the inflow velocity U_∞) corresponding to reference experimental results is investigated. Various body geometries are considered through the change of its width L (four aspect ratios L/H_s addressed) and its front edge curvature R (two rounded shapes R/H_s addressed). The combined effects of aspect ratio and curvature are considered by focusing on the vortex dynamics associated with the breakdown of the bubble through three-dimensional processes. Qualitative and quantitative comparisons with previous experiments are presented. The main influences of curvature and aspect ratio are consistently recovered in present simulations. The structure of the separation bubble is in agreement with experiments, especially the combination of singular points associated with the surface flow on the top-boundary of the body. Behind the separated region, the examination of the mean flow reveals the presence of a pair of longitudinal counter-rotating vortices pumping fluid from the side of the body to the top of the flow. The analysis of instantaneous visualizations shows the formation of strong lambda vortices for small aspect ratios. These vortices cause ejection of the fluid through a periodic bursting process which seems to be linked to the flapping of the separation bubble. The increase of the curvature of the rounded front edge is found to increase the separation angle, in qualitative agreement with experiments, with a global growing of the size of the separation bubble. The sensitivity of the flow to upstream conditions is discussed by considering different levels of inflow fluctuations (with a root mean square from zero to 1% of U_∞) while evaluating the deterministic response of the bubble dynamics with respect to cyclic inlet excitation. Strong curvature is found to reduce drastically the upstream receptivity of the flow, the resulting phenomena being interpreted in terms of convective/absolute stability.

1. Introduction

Most of bluff bodies (like cars, trains or buildings) have rounded edges that lead to regions where the flow separates and reattaches. Many other relevant cases are found in the field of aircraft aerodynamics, where flow separation can occur over high-lift wing for instance. The formation of separation bubbles causes the presence of eddying wakes in near-body region of the flow. The unsteady nature of the resulting vortex dynamics is of practical importance in many applications where noise emissions or structure vibrations have to be reduced through a passive or active control. For the flow over an airfoil, lift and drag are directly connected to the separation dynamics with important consequences on the efficiency and stability of the aircraft.

Separation bubble can be triggered by adverse pressure gradient without a direct influence of the curvature surface. However, in many applications mentioned above, curvature effects of the wall geometry can modify significantly the appearance of the separation bubble as well as its final shape and size. The present study focuses on the latter type of effects that remains significantly less studied than the single influence of a given pressure distribution over a quasi-planar surface. Moreover, because most of the separation bubbles are three-dimensional (3D) in practical flow geometries (Tobak and Peak, 1982), it is worth considering the influence of the aspect ratio of the body in cross direction. Consequently, the main goal of this study is to better understand how the combined effects of curvature and aspect ratio can select a different dynamics in the separation bubble zone, near the reattached zone (where a breakdown to turbulence can be observed) as well

---

* Corresponding author. Fax: +33 5 49 49 69 68.
E-mail addresses: lamballais@univ-poitiers.fr (E. Lamballais), jorgehs@pucrs.br (J. Silvestrini), s.laizet@imperial.ac.uk (S. Laizet).

0142-727X/$ - see front matter © 2008 Elsevier Inc. All rights reserved.
doi:10.1016/j.ijheatfluidflow.2008.03.006

as further downstream. In such complex flow geometry leading to a strong lateral expansion, curvature and pressure gradient both contribute to the formation and the dynamics of the separation bubble through physical mechanisms that need to be clarified. For this purpose, several flow configurations, already studied experimentally, are reproduced here by direct numerical simulation (DNS) and analysed by focusing on the role played by the various vortical structures involved in the bubble dynamics.

The organisation of this paper is as follows. Section 2 presents the physical configuration and its numerical modelling through the DNS methodology proposed here. The main features of the mean flow in the separated region as well as further downstream are analysed in Sections 3 and 4. The vortex dynamics associated with the main unsteady processes is discussed in Section 5. Then, the question of the receptivity of the flow with respect to inflow perturbations is addressed in Section 6. Finally, after a discussion in Section 7 on the analysis difficulties of upstream/downstream influence for a fully non-linear dynamics, the main results of this study are recalled in the concluding Section 8.

2. Flow parameters and numerical modelling

2.1. Flow configuration

Measurements (visualization, PIV, hot-film) have been conducted by Courtine et al. (2004, 2006, 2007) for a constant flow (of velocity U_∞) over a generic bluff body with different front edge radii and cross frontal sections. The model geometry and its parameters R, H_s, L and l are presented in Fig. 1. Using a low-speed water tunnel, Courtine et al. (2004, 2006, 2007) have considered flow regimes at moderate Reynolds numbers ($O(10^3) < Re = u_\infty H_s/\nu < O(10^4)$) so that a comparative work using DNS can be performed.

To be as close as possible to the experimental conditions, the cross section of the computational domain fits exactly the experimental one. However, to avoid the description of the lowest region of the water tunnel where an elevated ground plane was used (to limit the ground effect while considering a uniform flow in front of the obstacle), only the upper part of the flow above the horizontal plane (x, z) including the stagnation point is considered in present DNS. This particular plane is assumed to correspond to a free-slip wall where all the streamlines are purely horizontal (impermeable condition). Numerically, this assumption offers the advantage to ignore the complex experimental geometry near the ground while not having to prescribe a boundary layer at the inflow section. Due to the mirror symmetry associated with the presence of this free-slip wall at $y = 0$, the present numerical model can also be viewed as a full body with a perfect correlation between both flow dynamics on each of its sides $y > 0$ and $y < 0$. Then, using the location of the stagnation point reported by Courtine et al. (2004, 2006, 2007), the height of the half-body actually taken into account in present calculations is $H_s = 0.82H$ (see Fig. 2) while its length $l = 12H_s$ is extended to the exit section $x = L_x$ (semi-infinite body).

2.2. Numerical methods

The incompressible Navier–Stokes equations are solved using a numerical code (called "Incompact3d") based on sixth-order compact schemes for spatial discretization and second order Adams-Bashforth scheme for time advancement. The computational domain $L_x \times L_y \times L_z = 20H_s \times 5H_s \times 12H_s$ is discretized on a Cartesian grid (stretched in y) of $n_x \times n_y \times n_z = 601 \times 151 \times 401$ mesh nodes, except for the validation calculations where an extended domain and resolution is used in y-direction (see Section 2.4 for more details). To treat the incompressibility condition, a fractional step method requires to solve a Poisson equation. This equation is fully solved in the spectral space via the use of relevant 3D Fast Fourier Transforms that allows us to consider all the combinations of free-slip, periodic or Dirichlet boundary conditions on the velocity field in the three spatial directions. In present calculations, boundary conditions are only inflow/outflow in x (velocity boundary conditions of Dirichlet type), free-slip in y and free-slip or periodic in z. The pressure grid is staggered from the velocity grid to avoid spurious pressure oscillations. With the help of the concept of modified wave number, the divergence free condition is ensured up to the machine accuracy. More details about the present code and its validation, especially the original treatment of the pressure in the spectral space, can be found in Laizet (2004) and Laizet and Lamballais (submitted for publication), while some recent results obtained with the new version of "Incompact3d" are reported in Laizet and Lamballais (2005, 2006) and Laizet et al. (2007).

The modelling of the body is performed by an immersed boundary method (IBM). Following the procedure proposed by Parnaudeau et al. (2003), the present IBM is a direct forcing approach that ensures the no-slip boundary condition at the wall while creating an artificial flow inside the body. This internal flow, without physical significance, allows better regularity of the velocity field across the immersed boundary, this property being of primary importance when numerical schemes of spectral or quasi-spectral accuracy are used. Combined with a sixth-order compact filtering

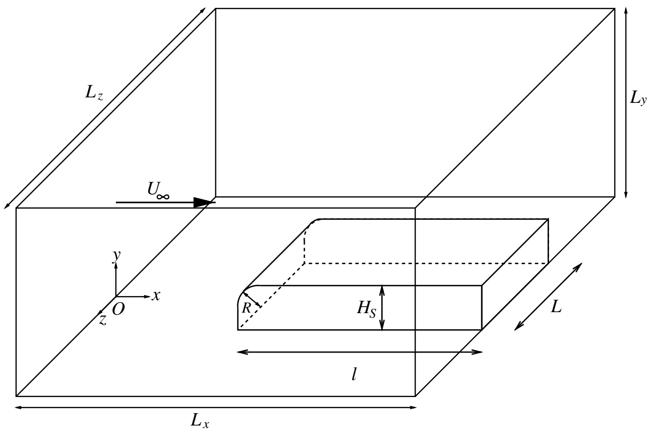

Fig. 1. Schematic view of the flow configuration.

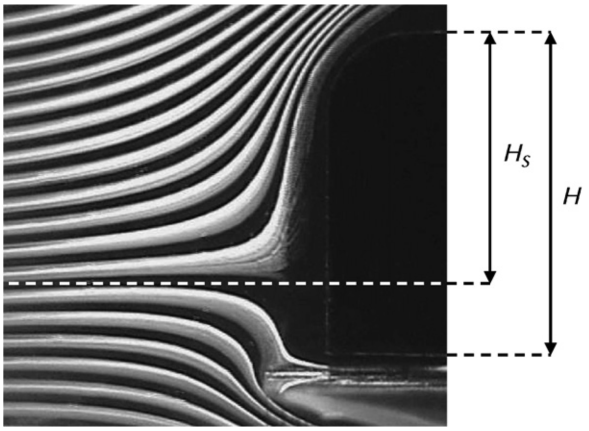

Fig. 2. Relation between the height of the half-body H considered by Courtine et al. (2004, 2006, 2007) and its corrected value H_s used in present DNS (stagnation point located in the lower horizontal boundary of the computational domain $y = 0$).

of the convective terms, this specific IBM leads to a reduction of wiggles in the neighbourhood of the body while allowing better quantitative predictions at marginal resolution (see Parnaudeau et al., 2003 for more details).

2.3. Physical and numerical parameters

The aim of this study is to investigate the influence of the aspect ratio $\Lambda = L/H$ and the non-dimensional rounded edge radius $\eta = R/H$. The cases $\Lambda = 2.2, 4.4, 8.8$ and $\eta = 0.8, 0.4$ are considered for $Re = 1250$, these specific flow configurations being well referenced in the database of Courtine et al. (2004, 2006, 2007). Note that to make easier comparisons with these experiments, the same definitions of Λ and η are used, based on H instead of H_s. To better identify the specific 3D effects associated with the moderate values of the aspect ratios, the case $\Lambda \to \infty$ is also considered using $L = L_z$ and $n_z = 400$ while the free-slip boundary condition is replaced by a periodic one in z-direction, this limit case corresponding to the body configuration considered by Yang and Voke (2001) using large eddy simulation (LES).

In addition to validation calculations, eight basic simulations have been conducted by considering the combinations of η and Λ reported in Tables 1 and 2. For each calculation, the flow has reached a developed state after an initial period of $120H_s/U_\infty$ computed using a coarser grid followed by a transient stage of $20H_s/U_\infty$ at the finest spatial resolution. All the instantaneous results presented in this paper are extracted from a subsequent temporal sequence of $20H_s/U_\infty$. Statistical data are computed using a time average over three times this duration ($60H_s/U_\infty$). For the case $\Lambda = \infty$, statistics are also averaged in the homogeneous z-direction in order to improve the convergence level. Exactly the same inlet conditions are used for the eight basic simulations.

In practice, the constant inflow velocity U_∞ is perturbed by fluctuations corresponding to a time and spatial correlated noise (of large band-width spectrum with an integral lengthscale of about $1.7H_s$) with a root mean square amplitude $u'_{\text{inflow}} \approx 1\%U_\infty$ consistent with the residual perturbations inside the working section of the wind tunnel used by Courtine et al. (2004, 2006, 2007). In Section 2.4 as well as in Section 6, complementary cases with no ($u'_{\text{inflow}} = 0$) or low ($u'_{\text{inflow}} \approx 0.1\%U_\infty$) inlet excitation are also reported. An important feature of these synthetic inflow fluctuations is that they have been randomly generated in the spectral space (using Fast Fourier Transform procedures) with a prescribed spectrum and a time periodicity $T = 20H_s/U_\infty$. For this reason, the instantaneous flows at the begin and the end of a given inflow cycle are strongly correlated in the region highly sensitive to inflow conditions. This characteristic will be discussed in Section 6 dedicated to the receptivity of the flow with respect to the inlet excitation.

To end this section, the relationships between statistical convergence and cyclic nature of the inflow excitation should be clarified. In fact, even if a large number of inflow cycles were used, the corresponding statistical convergence would remain linked to the content of the cycle itself. Consequently, despite the random nature of present cyclic inflow conditions, their periodicity prevents a time average procedure to converge toward ensemble average data. In other words, the ergodicity cannot be expected even if the time average is based on a infinite duration. The additional required condition for ergodicity would be the use of periodic inflow conditions over an infinite duration. As a time periodicity $T = 20H_s/U_\infty$ is used here, the statistics can only be considered converged with respect to this limited time sequence. In the region of the flow highly conditioned by inlet conditions, this type of convergence can be reached using a single cycle for the average in time, while several cycles can be useful to improve the convergence in less deterministic regions. A compromise of three cycles for the basic statistics has been made in this paper. Indeed, preliminary statistical comparisons from one cycle to another have shown that the level of convergence can be considered satisfactory, as far as our interpretations are concerned. For finite Λ cases, the analysis of the mean flow symmetry with respect to the plan $z = 0$ has confirmed this choice. Finally, it should be noted that this convergence drawback of the use of cyclic inflow conditions will be turned advantageously in the receptivity analysis presented in Section 6.

Table 1
Reattachment length for each case

Λ	2.2		4.4		8.8		∞	
η	0.4	0.8	0.4	0.8	0.4	0.8	0.4	0.8
h_r/H_s	0.39	0.32 (0.40)	0.48	0.40	0.43	0.32	0.38	0.27
l_r/H_s	2.70	2.45 (3.5)	3.34	3.26	3.50	3.51	3.07	3.25
Exp.	2.9	2.8	–	3.4	–	3.9	–	–

The values between brackets correspond to the DNS performed without inflow perturbations. Experimental measurements are from Courtine et al. (2004, 2006, 2007).

Table 2
Distance d_f between separation foci for each case

Λ	2.2		4.4		8.8		∞	
η	0.4	0.8	0.4	0.8	0.4	0.8	0.4	0.8
d_f/H_s	2.41	2.05 (2.32)	4.71	4.42	10.09	9.35	–	–
d_f/l_r	0.89	0.84 (0.66)	1.41	1.36	2.88	2.66	–	–
Exp.	–	0.62	–	1.2	–	2.1	–	–

The values between brackets correspond to the DNS performed without inflow perturbations. Experimental measurements are from Courtine et al. (2004, 2006, 2007).

2.4. Preliminary comparisons with previous LES results

The only referenced DNS/LES study found by the authors about the flow over a two-dimensional (2D) rounded bluff body corresponds to the LES of Yang and Voke (2001), while no results issued from present 3D body (i.e. for finite aspect ratio Λ) seem to be available in the literature. Among present eight basic DNS, the case $\Lambda = \infty$ and $\eta = 0.8$ leads to $H_s = 0.97R$ which is very close to the body geometry of Yang and Voke (2001) where the curvature radius corresponds exactly to the height of the half-body, namely $H_s = R$.

The size of the bubble through its longitudinal expansion is considered as first comparison. The associated parameter is called the reattachment length l_r that measures the distance from the location of the separation (occurring nearly just upstream from the end of the body curvature, at $x_0 = L_x - l + R$ for the present geometrical parameters) to the position where flow reattaches. Here, as it is mentioned in Table 1, a value $l_r = 3.25H_s$ is obtained against the value $l_r = 5.2H_s$ reported by Yang and Voke (2001) in good agreement with the experimental value of J. Coupland ($l_r = 5.5H_s$) mentioned by the same authors.

Note that in terms of spatial resolution, compared with the LES of Yang and Voke (2001), present DNS is based on a significantly larger number of mesh nodes but with a different grid organization (Yang and Voke (2001) have used a fully general coordinate system) over a computational domain three times more extended in spanwise direction for the present work. Expressed in wall units based on the friction velocity of the boundary layer at a distance $1.5l_r$ downstream from the reattachment, the streamwise and spanwise mesh sizes are $\Delta x^+ \approx 4$ and $\Delta z^+ \approx 3.5$ respectively, while at the top surface of the body, the normal grid spacing is $\Delta y^+ \approx 3$.[1] These values suggest that the grid is compatible with a DNS approach despite the use of a marginal near-wall normal resolution that can be supported here with the help of high-order schemes (Laizet and Lamballais, submitted for publication).

In order to understand the reasons of this strong discrepancy between present results and these reference ones, a confined effect has been suspected first. It would be due to the closeness of the top free-slip wall at $y = L_y$ which leads to a significantly higher blockage ratio compared with the reference one (1:5 in this work and 1:16 in the LES study of Yang and Voke, 2001). To better evaluate the role of the blockage ratio on the bubble length, the same DNS has been performed with an extended computational domain in y (with $L_y = 16H_s$) and an adapted y-resolution ($n_y = 201$ with a stretching calibrated to ensure a similar resolution near the body). Despite this use of the same blockage ratio as Yang and Voke (2001), a strongly underestimated value of $l_r = 3.6H_s$ has been again obtained. Note that the present behaviour suggests that a blockage ratio of 1:5, despite its high value, has a moderate effect on the size of the bubble, the resulting underestimation being only 10%.

The second major difference between present DNS and previous LES or experiments is related to the level of free-stream turbulence. In the eight basic DNS presented here, the inflow perturbation level has been adjusted on the reference experiments of Courtine et al. (2004, 2006, 2007) with $u'_{\mathrm{inflow}} \approx 1\% U_\infty$, this somewhat high amplitude being related to the use of a low speed water tunnel. In LES and experiments reported by Yang and Voke (2001), the turbulence level is significantly lower with $u'_{\mathrm{inflow}} \approx 0.1\% U_\infty$. In consequence, an additional DNS has been performed based on the large computational domain ($L_y = 16H_s$) but with inflow perturbations reduced by a factor 10 (namely the same free-stream turbulence level than Yang and Voke (2001)). In this third case, the value $l_r = 5.5H_s$ is obtained, in excellent agreement with both LES and experiments reported by Yang and Voke (2001).

This high sensitivity of the reattachment length with respect to the level of inlet excitation suggests a strong receptivity of the bubble dynamics with respect to inflow condition, a typical characteristic of convectively unstable flow. To confirm this behaviour, a fourth DNS has been conducted based again on the y-extended computational domain but free from any inlet excitation ($u'_{\mathrm{inflow}} = 0$). For this calculation, the initial condition corresponds to a fully established flow with inflow perturbations. The resulting behaviour of the flow leads to a continual increase of the bubble length up to $l_r > 9H_s$. As the computational domain is too short in x to simulate correctly a longer bubble (the errors introduced by the outflow boundary conditions would lead to doubtful conclusions), this DNS has been stopped. However, this gradual increase of the bubble length is in contradiction with the observations of Yang and Voke (2001) who reported that disturbances are only required at the start of the simulation, the following bubble dynamics being found to be self-sustaining without any inflow excitation, with minor effects (less than 3%) on the prediction of significant quantities. No relevant explanation has been found about this discrepancy between present DNS and previous LES when no inflow disturbances are introduced. However, the observation in the absence of any free-stream perturbation seems to confirm that the flow exhibits characteristics of convective stability, so that present behaviour seems to be consistent.

In the rest of this paper, the results issued from present additional DNS (enlarged computational domain and weak inlet excitation) will not be considered, the main validation strategy consisting in the direct comparisons between experiments of Courtine et al. (2004, 2006, 2007) and present results in flow configurations as closed as possible from each other.

3. Main features of the separation bubble

Here, as in the rest of the paper, the region of the flow above the body is specifically studied. Then, all that is discussed in the following mainly concern the dynamics near the upside of the body ($y > H_s$) without considering the motions near the edges ($z < -L/2$ or $z > L/2$). To have a complete view of the flow, the dynamics found in these lateral zones can be distinguished in some figures presented here but is not explicitly commented on.

The longitudinal expansion of the separation bubble can be considered through the reattachment length l_r that corresponds to the maximum of the x-location where the time-averaged mean flow reattaches. The same definition as Courtine et al. (2004, 2006, 2007) is used here, without taking exactly the separation location (occurring near $x_0 = L_x - l + R$ as already mentioned) into account to measure l_r. For flow configurations with finite Λ, this maximum value is found in the plane of symmetry $z = 0$ while for $\Lambda = \infty$, due to the homogeneous character of the flow in z-direction, l_r can be deduced in any z.

Four examples of separation bubble viewed in a vertical section are presented in Fig. 3 where streamlines associated with the mean velocity field are plotted. Note that after statistical convergence, these streamlines should be the true ones without any projection, because the mean flow is purely 2D for $\Lambda = \infty$ while for finite Λ, the vertical section is taken at $z = 0$. This plane corresponds to a plane of mirror symmetry for the mean flow where the spanwise mean velocity is expected to be zero ($z = 0$ can be viewed as a vertical free-slip wall for the statistically converged mean flow). The streamline patterns obtained for finite or infinite Λ are observed to be of different nature, as it can be expected. More precisely, since the mean flow is incompressible, the streamlines associated with the 2D mean flow are found to correspond to characteristic lines of an incompressible field where streamlines form closed loops inside the bubble. Note that same streamlines can also be recovered by plotting isocontours of the stream function associated with the 2D mean flow, confirming the fact that streamlines are closed loops inside the bubble. Topologically, the centre of a 2D bubble corresponds to a singular point (of zero velocity) that is classified as a focus that is neither divergent nor convergent, so that it is commonly called “centre” (see for instance the reviews of Tobak and Peak, 1982; Delery, 2001, for more detailed about flow topology). For the case $\Lambda = 2.2$, as for any other finite Λ case, the centre of the bubble remains a focus, but it can be this time divergent or convergent. The reason is that the (x, y)-projected mean velocity $(U, V, 0)$, despite $W = 0$ in $z = 0$, is not necessary divergent free in this particular plane due to the possible spanwise gradient of the spanwise mean velocity. In other words, for finite Λ cases, $\mathrm{d}U/\mathrm{d}x + \mathrm{d}V/\mathrm{d}y \neq 0$ when $\mathrm{d}W/\mathrm{d}z \neq 0$, even if $W = 0$ like in the plane $z = 0$. It should be noted that the central region of the bubble (viewed in the section $z = 0$) is found to be a zone of positive divergence, in a way that the core of the bubble is corresponding to a divergent focus instead of a centre. Physically, it means that the bubble core is alimented by fluid that converges toward the plane $z = 0$ each side of this plane.

The values of l_r obtained in each case are given in Table 1. A good agreement is found with Courtine et al. (2004, 2006, 2007) for the four flow configurations reported by these authors. The strongest discrepancy concerns a case with $\Lambda = 8.8$ where it can be expected that the present use of free-slip boundary conditions at $z = \pm L_z/2$ is not realistic enough compared with the no-slip side walls of the wind tunnel used by Courtine et al. (2004, 2006, 2007).

---

[1] Similar mesh sizes in wall units are obtained for the other flow configurations with $\Lambda = \infty$.

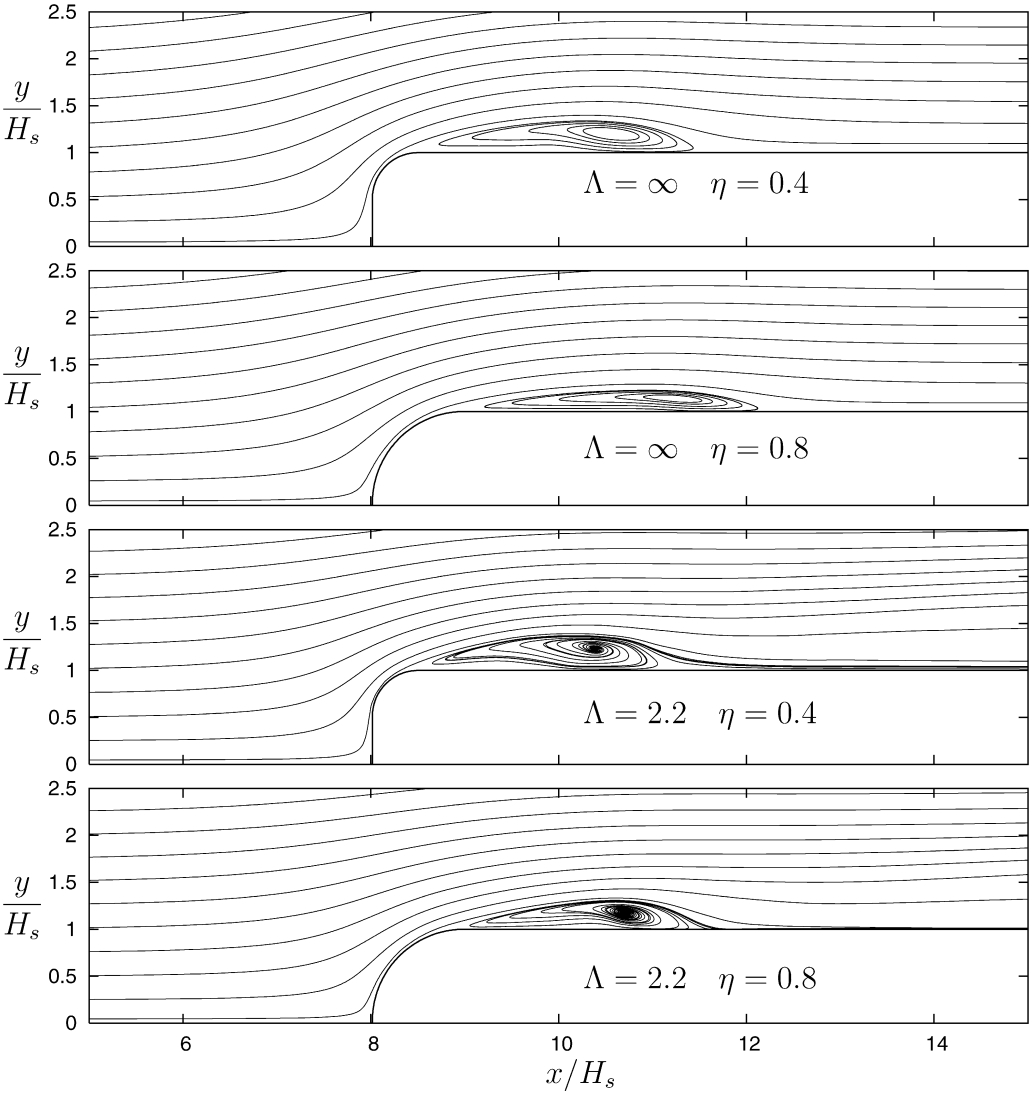

Fig. 3. Mean streamlines in $z = 0$ section for $\Lambda = 2.2, \infty$ and $\eta = 0.4, 0.8$.

The side walls are located here at a short distance of $(L_z - L)/2 = 0.63H_s$ from the edges of the body, so that their different effects, depending on their free-slip (DNS) or no-slip (experiments) nature, can significantly influence the dynamics in the near-body region. Despite this reservation, it should be noted that the present increase of l_r with Λ is consistent with experiments. However, for $\Lambda = \infty$ (where no experiment is reported), a slight decrease can be observed by comparison with $\Lambda = 8.8$. This behaviour can be interpreted as a consequence of the blockage ratios which are 1:27, 1:14, 1:7 and 1:5 for $\Lambda = 2.2, 4.4, 8.8, \infty$ respectively. The effects of η on l_r seems to be rather limited, with a more marked influence on the shape of the separation bubble through its height h_r that is higher at $\eta = 0.4$ than at $\eta = 0.8$ for all the cases considered here (see Table 1). An example of this effect can be seen in Fig. 3 where the increase of the height bubble is found to be mainly related to the increase of the separation angle. Once again, due to the blockage effect that depends on Λ, it is not possible to establish a clear influence of Λ on the height h_r.

The structure of the separation bubble can be characterised by the analysis of the skin-friction lines on the surface. Fig. 4 presents the mean streamlines in the neighbourhood of the top of the body with $\eta = 0.8$ and $\Lambda = 2.2$. For this case, the flow pattern immediately adjacent to the surface reveals the presence of six singular points. At the centre $z = 0$ of the separation line, one saddle point can be identified. Slightly further downstream, to close the separation line near each edge of the body, two foci of separation are clearly observed. Finally, one nodal attachment point located between two saddle points ends the bubble. This surface flow pattern, corresponding to a stable configuration as described by Perry and Chong (1986), is in agreement with the measurements of Courtine et al. (2004, 2006, 2007) who identified the same type of surface flow topology at this near-wall location. A quantitative comparison between present DNS and previous experimental results is proposed in Table 2 where the distance d_f between the two separation foci is considered. For the cases $\Lambda = \infty$, the separation is 2D so that only two separation and reattachment lines can be expected after the full statistical convergence. For the other cases, the structure of the surface flow is qualitatively similar near the separation (one saddle plus two foci points) but further downstream, the lack of convergence (the time average is only based on $60H_s/U_\infty$) does not allow us to identify clearly the singular points near the reattachment for the cases $\Lambda = 4.4, 8.8$. In practice, the clear identification of singular points in the reattached region seems to be more stringent in terms of statistical convergence

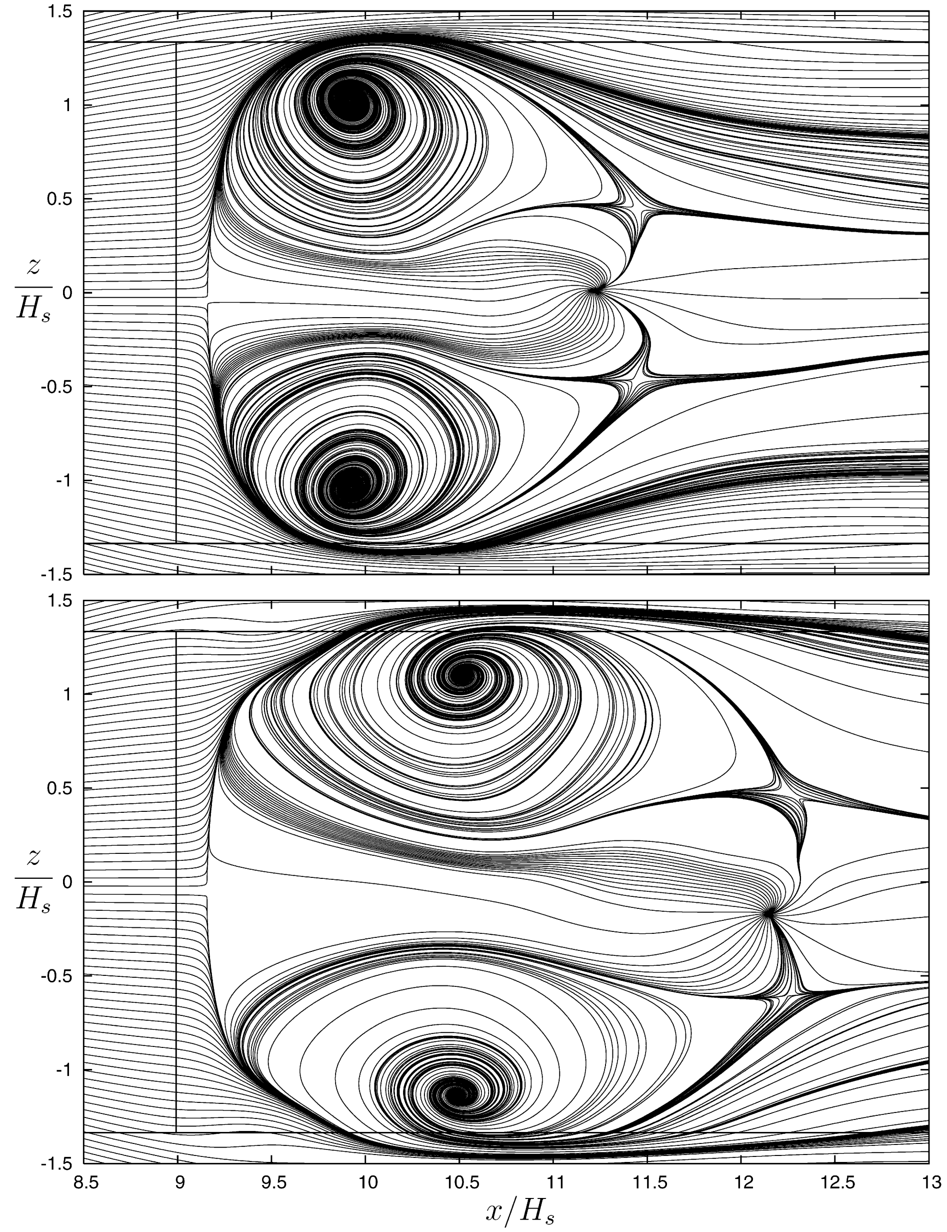

Fig. 4. Mean streamlines in the plane $y = 1.06H_s$ for $\Lambda = 2.2$ and $\eta = 0.8$ with (top) and without (bottom) inflow perturbations. No symmetry is applied with respect to the axis $z = 0$.

for high aspect ratio, especially at $\Lambda = 8.8$. Consequently, it would be necessary to perform a very long DNS to exhibit the flow topology near the reattachment for high Λ cases, this requirement being considered here too computationally expensive regarding the main goals of the present study.

Finally, let us mention that the foci are found to be divergent for the eight DNS. To our knowledge, this topology is unusual (without being non-physical), the typical foci inside 3D separation being described as convergent in the literature (Tobak and Peak, 1982; Delery, 2001; Perry and Chong, 1986). The divergence of present foci involves that no streamline issued from upstream can reach a focus and then enters inside the bubble. This behaviour can be clearly observed in Fig. 4. The divergence of present foci and the resulting impossibility for any streamline emitted in front of the body to enter into the bubble are not recovered in the experiments of Courtine et al. (2004, 2006, 2007) while not being exhibited by Perry and Chong (1986) in their theoretical surface flow patterns based on the same combination of singular points. More investigation seems to be necessary to understand the reason of this fundamental difference.

4. Mean flow behind the reattachment

The analysis of the mean velocity field shows that behind the separation bubble, in agreement with the usual description of 3D separated/reattached flows, the mean flow remains highly 3D with the presence of a counter-rotating pair of longitudinal vortices that tend to pump fluid from the sides toward the plane $z = 0$ where the fluid is ejected toward the top of the domain. These two mean longitudinal vortices cannot be detected using classical criteria for vortex identification. It is due to their very large scale component that is not well captured by an identification scheme based on velocity derivatives (like vorticity or the Q quantity). For this

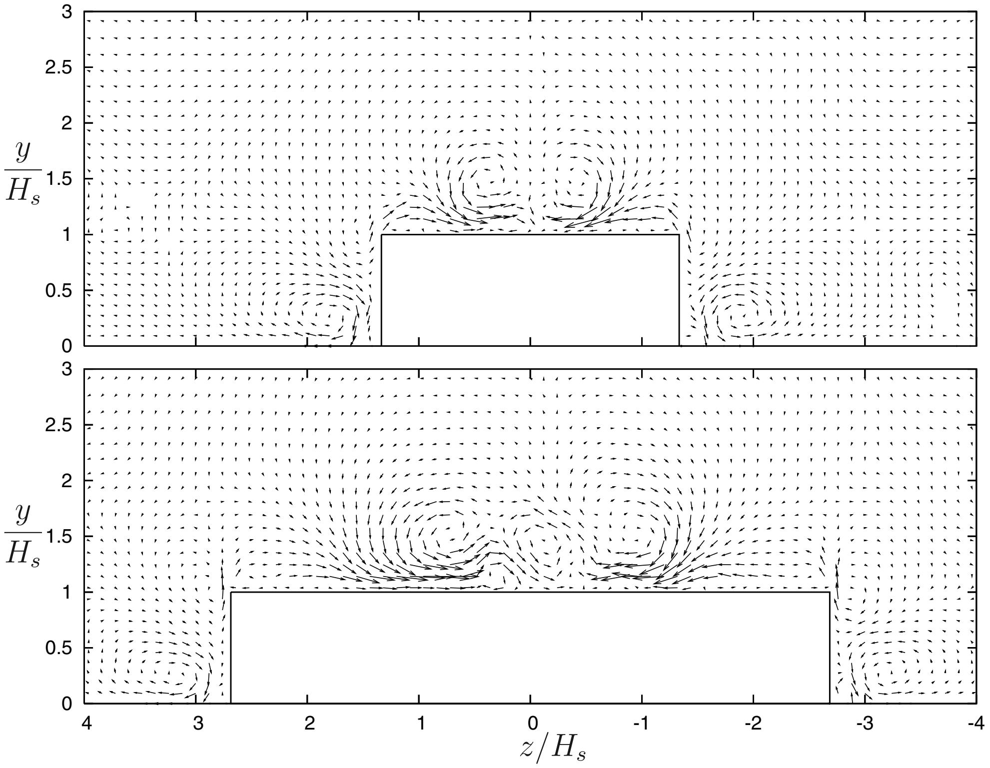

Fig. 5. Velocity vectors (w, v) in $(x - x_0)/l_r = 1.5$ for $\eta = 0.8$ with $\Lambda = 2.2$ (top) and $\Lambda = 4.4$ (bottom). No symmetry is applied with respect to the axis $z = 0$.

reason, the velocity vectors in a (z, y) section downstream from the separation bubble are directly plotted. As the presence of longitudinal structures cannot be clearly identified for $\Lambda = 8.8$ (due to the lack of convergence), only two cases are compared in Fig. 5 for $\Lambda = 2.2, 4.4$ with $\eta = 0.8$ (the corresponding cases $\eta = 0.4$ lead to similar conclusions). In this figure, the presence of two counter-rotating longitudinal vortices can be clearly observed. The location of each vortex pair is near the symmetrical plane $z = 0$ for $\Lambda = 2.2$ as well as for $\Lambda = 4.4$. The characteristic velocities induced by these structures are rather high ($w_{\max} = 12\%, 15\% U_\infty$ for $\Lambda = 2.2, 4.4$ respectively at the section presented in Fig. 5) so that an efficient pumping effect (from the sides to the top) remains present at $(x - x_0)/l_r = 1.5$ (the maximum values of lateral currents are found inside the separation bubble with $w_{\max} = 29\%, 36\% U_\infty$ for $\Lambda = 2.2, 4.4$ respectively). Because this analysis is only based on the mean flow, it is not possible to have an idea about the unsteady processes that are responsible for these phenomena. This point is the main subject of the next section.

5. Vortex dynamics

This section focuses on the combined influences of Λ and η on the vortex dynamics associated with the separation and reattachment. To identify the vortical motions, the Q-criterion is used because it gives clearer instantaneous visualizations than vorticity for the present flow, especially in the region where instabilities are triggered (see Lesieur et al., 2005, for a review of coherent vortex identification and illustrated examples). For the nine DNS presented here, the full animation of Q-visualizations has been performed, using 200 velocity fields saved with a period of 0.1 H_s/U_∞. Some typical instantaneous visualization are presented in Figs. 6–9 and 11.

As a first conclusion, the observation of the animations shows that in the neighbourhood of the separation line, the flow remains almost steady for the nine cases considered here, consistently with the experiments of Courtine et al. (2004, 2006, 2007). Further downstream, the separation leads to the formation of an unstable shear layer where Kelvin–Helmholtz vortices form and roll-up through 3D processes. The frequency f associated with the formation of Kelvin–Helmholtz vortices leads to Strouhal numbers $St = fH_s/U_\infty$ consistent with the data of Courtine et al. (2004, 2006, 2007) (for instance, $St \approx 0.6$ here and $St = 0.58$ in experiments for $\Lambda = 2.2$ and $\eta = 0.8$). However, the present uncertainty on f (due to the limited duration of DNS) prevents us to analyse in more detail St in various cases.

As it can be expected, when Λ is increased, Kelvin–Helmholtz structures are found to be more 2D, but no significant acceleration or slowdown of primary instabilities can be noticed. Further downstream, strong distortions of primary structures occur and streamwise vortices are quickly formed by stretching. This scenario is recovered for the nine cases considered here, the appearance of 3D mechanisms being slightly favoured by a body with small Λ and somewhat inhibited by a 2D body with $\Lambda = \infty$. In the latter case, the breakdown to turbulence seems to suddenly occur near the reattachment zone.

In terms of vortex dynamics, the main effect of Λ is found to be related to the shape of the typical vortical structures that develop in the separation bubble. For $\Lambda = 2.2$, a flapping of the separation bubble is observed, the resulting motion leading to a highly 3D dynamics composed of periodic eruption of fluid in the middle plane $z = 0$. These phenomena are linked to the periodic formation of large scale lambda structures. The stretching by the mean flow reinforces these hairpin vortices that are also submitted to self-induction effects that tend to create strong ejection through bursting processes similar to the ones described in turbulent wall flows. These lambda structures have already been experimentally identified by Courtine et al. (2004, 2006, 2007) as mushroom shaped structures in cross section visualizations. For higher values of Λ,

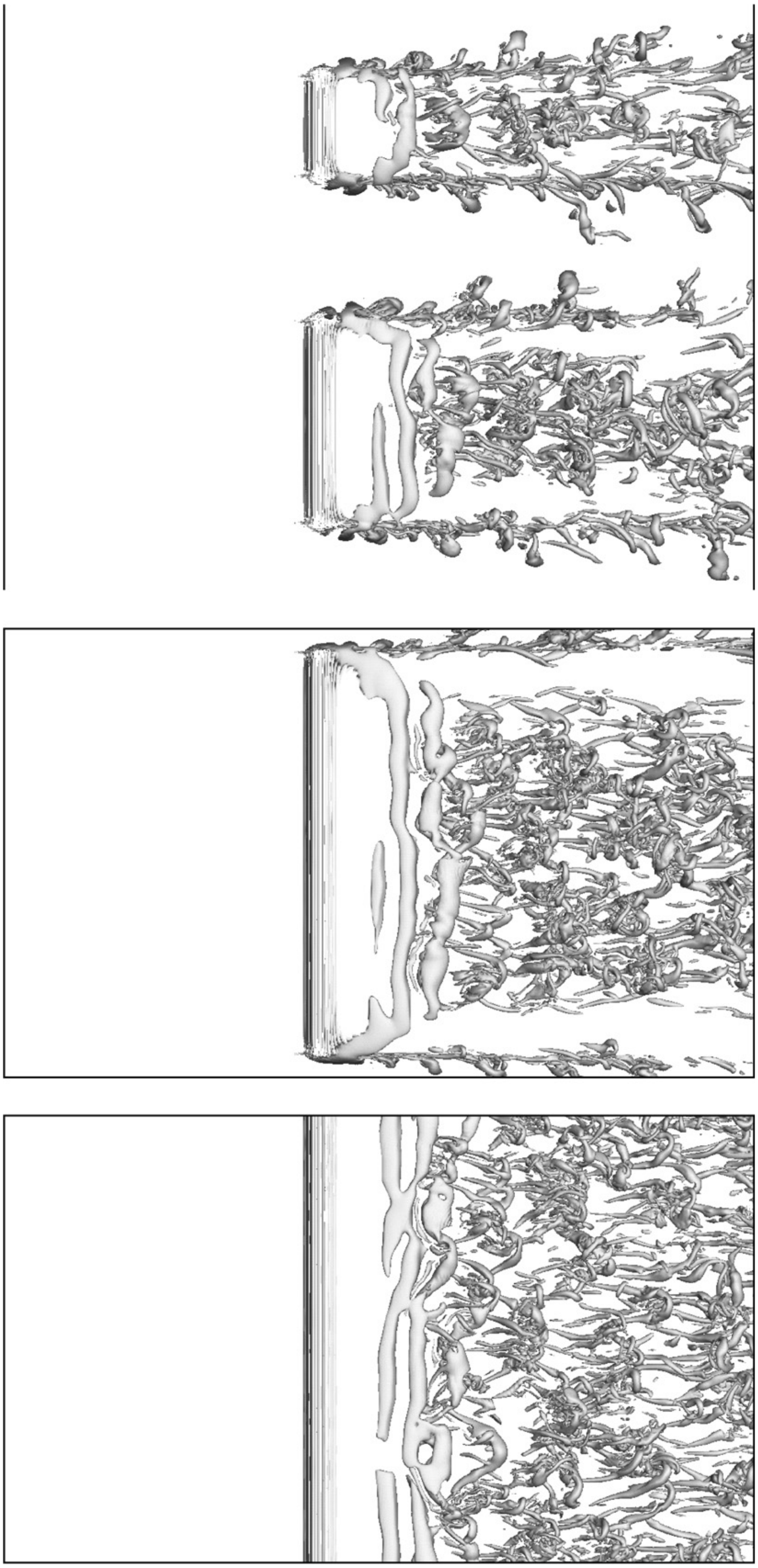

Fig. 6. Top views of the isosurface $Q = 0.25U_\infty^2/H_s^2$ for $\eta = 0.8$ with $\Lambda = 2.2, 4.4, 8.8, \infty$ ($u'_{\text{inflow}} \approx 1\%U_\infty$) from top to bottom (full computational domain only for the two cases with high Λ).

these particular large scale hairpin structures are progressively reduced and finally suppressed for the case $\Lambda = \infty$. The occurrence of marked ejections for $\Lambda = 2.2$ compared with the case $\Lambda = \infty$ can be observed in Fig. 7. These side views of the flow clearly show how the periodic ejections influence the growth of the boundary layer that develops over the body.

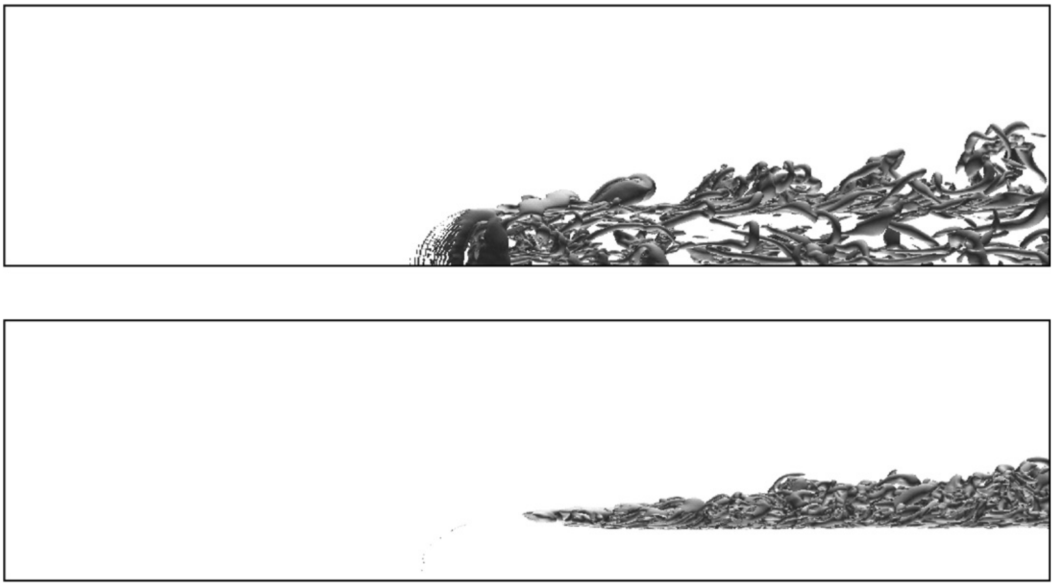

Fig. 7. Side views of the isosurface $Q = 0.25U_\infty^2/H_s^2$ for $\eta = 0.8$ ($u'_{\text{inflow}} \approx 1\%U_\infty$) with $\Lambda = 2.2$ (top) and $\Lambda = \infty$ (bottom).

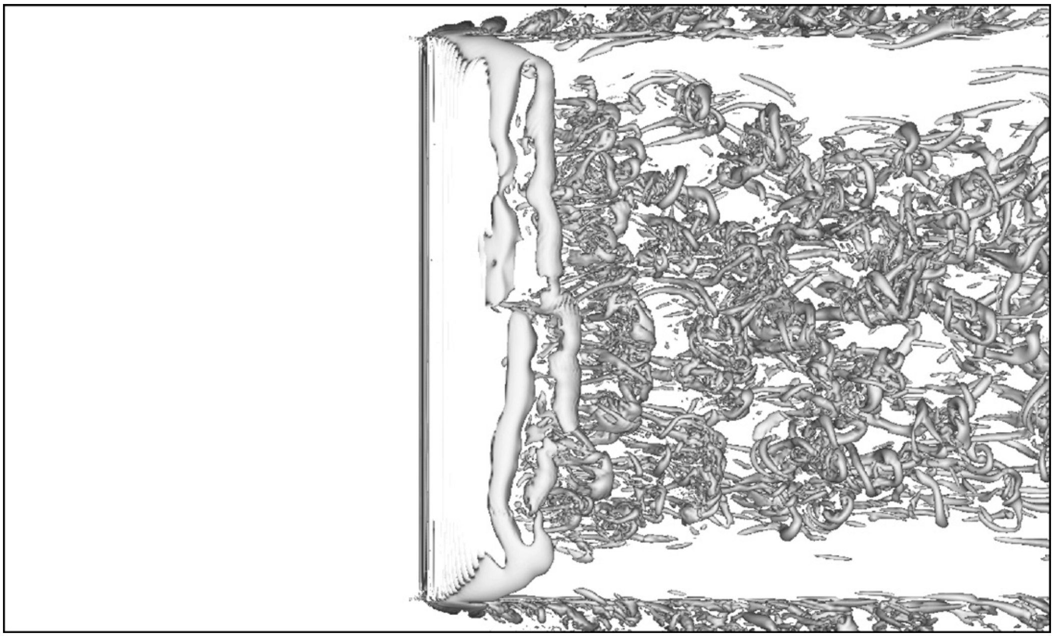

Fig. 8. Top view of the isosurface $Q = 0.25U_\infty^2/H_s^2$ for $\eta = 0.4$ and $\Lambda = 8.8$ ($u'_{\text{inflow}} \approx 1\%U_\infty$).

It seems reasonable to interpret the presence of the mean longitudinal vortices observed in the previous section as the signature of the present lambda vortices that cause central eruption of fluid alimented by a simultaneous lateral pumping of fluid from each side of the body. The reason of the creation of periodic large scale lambda vortices for the smallest aspect ratio $\Lambda = 2.2$ is probably linked to the closeness of the two foci (see Table 2 to compare the distance d_f between the foci for each case) for this flow configuration. Although the connection between foci and lambda vortices cannot be directly exhibited with visualization based on Q-criterion, the legs of lambda vortices seem to emerge from the foci that can interact when the aspect ratio of the separation bubble is small enough.

The effect of the curvature of the rounded edge on vortex dynamics can be considered by comparing the top views in Figs. 6 ($\eta = 0.8$) and 8 ($\eta = 0.4$). Only the case $\Lambda = 8.8$ is presented here, but similar conclusions can be drawn for the other aspect ratios. Here, the main effect is that the breakdown to turbulence is significantly accelerated for the case with the strongest curvature $\eta = 0.4$. More precisely, the triggering of primary instabilities are not strongly modified by the reduction of η, but the onset of 3D secondary instabilities clearly appears before the reattachment at $\eta = 0.4$. The resulting longitudinal vortices introduce small scale motions that cause an abrupt turbulent breakdown further downstream. Comparisons between Figs. 6 and 8 show that smaller vortices are excited by the use of a high curvature, so that the resulting flow seems to correspond to a higher Reynolds number case. It is important to recall that the Reynolds number based on H_s is the same for both flows, while the one based on R is twice smaller at $\eta = 0.4$. To interpret the mechanisms responsible of the appear-

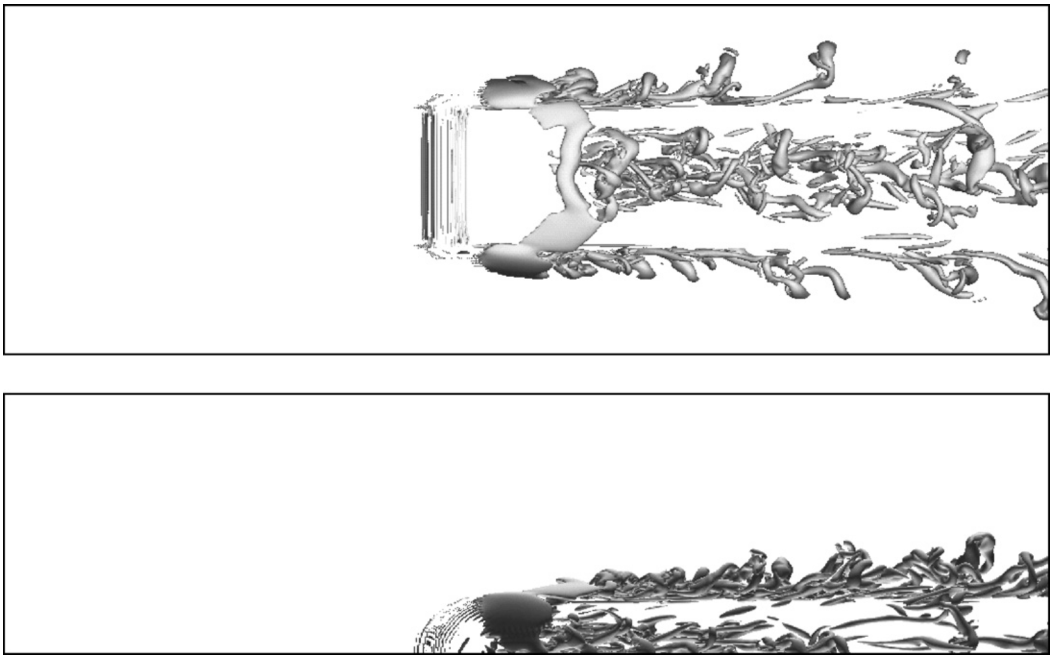

Fig. 9. Top and side views of the isosurface $Q = 0.25U_\infty^2/H_s^2$ for $\eta = 0.8$ and $\Lambda = 2.2$ for the DNS without inflow perturbations ($u'_{\mathrm{inflow}} = 0$).

ance of vortices at smaller scale, it does not seem relevant to propose a scaling with R through the definition of the Reynolds number or the direct normalization of the typical size of the vortices. A more interesting fact, already discussed previously, is that the separation angle tends to increase with decreasing η. The resulting modification of the shape of the separation bubble is susceptible to modify its characteristics in terms of convective/absolute stability. Without considering theoretically this delicate point, the careful observation of animations in the separation bubble shows that contrary to the case $\eta = 0.8$, small structures are continuously transported from the attachment region toward the separation line by the reverse flow in the bubble for the case $\eta = 0.4$. This behaviour suggests the possibility of a self-excitation mechanism, able to transmit 3D perturbations from the reattaching region to the separated shear layer and then trigger efficiently 3D secondary instabilities. This point will be considered indirectly in the next section through an analysis of the receptivity of the flow to inflow conditions.

6. Sensitivity to inflow conditions

6.1. Effect of the level of inlet excitation

The question of the receptivity to upstream conditions is very delicate to address experimentally. In their experiments done in a low-speed water tunnel, Courtine et al. (2004, 2006, 2007) were able to reduce to 1% the level of velocity fluctuations at the inlet of the test section for the lowest Reynolds considered ($Re = 1250$) that could be obtained with $U_\infty = 0.03\ \mathrm{m/s}$. In the present DNS methodology, it is possible to consider the same flow configuration without inflow perturbations, the residual ones corresponding to numerical errors of low amplitude. The goal of this method is to have a first idea about possible globally unstable nature (Huerre and Monkewitz, 1990; Chomaz, 2005) of present flows over 2D and 3D half-bodies.

In a first step, two additional DNS have been conducted by simply suppressing any inlet excitation ($u'_{\mathrm{inflow}} = 0$) for $\Lambda = \infty$ (2D bodies). This type of test, already discussed in the validation Section 2.4 for $L_y = 16H_s$ and $\eta = 0.8$, is simply repeated here for the standard computational domain ($L_y = 5H_s$) and for both curvatures $\eta = 0.4, 0.8$. For these two new cases, the behaviour of the bubble length is similar: l_r tends to gradually increase so that the reattachment zone becomes too close from the exit (we observe $l_r > 9H_s$) of the computational domain to carry on with confidence the calculation. If the same flow configurations are simulated using weak inflow perturbations ($u'_{\mathrm{inflow}} \approx 0.1\% U_\infty$), consistently with the preliminary validations in Section 2.4, the reattachment length can reach an established value that is significantly higher than for the standard inflow perturbations. For $\eta = 0.8$, a length $l_r = 4.91H_s$ (+51%) is obtained while $l_r = 4.51H_s$ (+47%) for $\eta = 0.4$. The strong receptivity of the separation bubble (considered here simply through the selection of its length) suggests that the flow remains dominated by convective instability mechanisms for these two configurations. Note however that the high curvature case is found to be slightly less sensitive to the level of inlet excitation than the low curvature case.

In a second step, one additional simulation has been performed, free from inflow perturbations by considering the case with the smallest aspect ratio $\Lambda = 2.2$ and the lowest curvature $\eta = 0.8$. The comparison of the behaviour of the flow with and without inflow perturbations can be done through the simultaneous examination of Figs. 6, 7 and 9. The first conclusion is that the flow remains unstable despite the lack of any excitation at the inlet of the computational domain. However, the primary instabilities are significantly delayed, so that the breakdown of the separation bubble is found to occur further downstream. Schematically, the separation bubble seems to be highly receptive to inlet perturbations in its upstream part while near the reattachment, transition processes are found to be self-sustaining. The possibility for a flow to be self-excited refers to absolutely unstable flows, but the sensitivity with respect to inflow fluctuations corresponds more to a characteristic of convective instability, so that it is difficult to conclude, even qualitatively, about the globally unstable nature of the present flow configuration. Naturally, the increase of the steady part of the separation bubble leads to a global increase of its longitudinal size but also of its vertical expansion (rises of 43% for l_r and

25% for h_r, see Table 1). Note that the bubble is found to be qualitatively similar with or without inflow perturbations (see Fig. 4 for a comparison between the two surface flow patterns). Further downstream, the flow near the reattaching zone becomes clearly unsteady so that a breakdown can be observed with the presence of vortical structures, similar in their form to the case with inflow perturbations, but significantly less numerous. This comparative test demonstrates the self-excited nature of the dynamics near the reattachment region. The fundamental reasons for the self-sustaining mechanisms need to be clarified, especially the importance of the 3D character of the body (because no efficient self-excitation mechanisms are observed for $\Lambda = \infty$) and the role played by the separations on the side of the body (behind the vertical sharp edges of the half-body) that could interact with the top separation bubble and then change its stability characteristics. A formal stability analysis could be interesting to better interpret these effects.

6.2. *Deterministic response of the bubble dynamics with respect to cyclic inlet excitation*

To evaluate the receptivity of the flow with respect to upstream conditions, a comparison between two sets of flow realizations is proposed here. They are obtained from the same DNS but for two different cycles of inflow conditions. Using the present type of inlet conditions that are random but purely periodic over the duration $T = 20H_s/U_\infty$, this type of analysis can be performed straightforwardly by comparing the instantaneous velocity field at the time t with its counterpart taken at the time $t + T$. This principle is illustrated in Fig. 10 that presents two maps of velocity fluctuations obtained for two consecutive cycles of inflow conditions. If a T-periodic inflow excitation would lead to a T-periodic flow, these two pictures should be identical. In practice, for the major part of the domain, which is the more convective one, the correlation between the two flow realizations is excellent, while in the near body region, some differences can be observed. The same type of comparison can be done using full 3D fields as it can be illustrated by comparison of Fig. 11 showing the initial state of the flow with Fig. 6 showing its final state $20H_s/U_\infty$ later. The similarity between these two instantaneous visualizations, related to the use of cyclic inflow excitations, can be easily observed in a significant upstream part of the computational domain. Downstream from a critical streamwise position, located in the separation bubble, the two flow realizations reveal small differences that grow continuously up to the outlet of the computational domain.

To have a quantitative estimation of this correlation level between two sets of flow realizations, a correlation coefficient $C(\mathbf{x}, T)$ is introduced here. It corresponds to a two-time correlation based on the fluctuating velocity field $\mathbf{u}'(\mathbf{x}, t)$, with formally

$$C(\mathbf{x},T) = \frac{\langle \mathbf{u}'(\mathbf{x},t)\cdot\mathbf{u}'(\mathbf{x},t+T)\rangle_t}{\sqrt{\langle \mathbf{u}'(\mathbf{x},t)^2\rangle_t}\sqrt{\langle \mathbf{u}'(\mathbf{x},t+T)^2\rangle_t}} \quad (1)$$

where the operator $\langle\cdot\rangle_t$ denotes a time average. Only the time separation T corresponding to the periodicity of inflow conditions is considered here. Note also that the vectorial nature of the expression (1) (where '·' indicates a scalar product) allows us to consider the three components of the velocity field in the statistics. The present correlation coefficient is defined to be equal to one in the region where the flow is purely T-periodic and zero where the flow does not have any T-periodicity. As the convergence of these statistics would require a very long time integration, only two cases are considered here, with a 2D body ($\Lambda = \infty$) in order to use the homogeneous z-direction to improve the statistical convergence, the associated correlation coefficient $C(x, y, T)$ being in this framework

$$C(x,y,T) = \frac{\langle \mathbf{u}'(\mathbf{x},t)\cdot\mathbf{u}'(\mathbf{x},t+T)\rangle_{t,z}}{\sqrt{\langle \mathbf{u}'(\mathbf{x},t)^2\rangle_{t,z}}\sqrt{\langle \mathbf{u}'(\mathbf{x},t+T)^2\rangle_{t,z}}} \quad (2)$$

where the operator $\langle\cdot\rangle_{t,z}$ denotes an average in time and also in z. In practice, to compute this coefficient, the data has been averaged on the duration of one cycle T by using 2×100 velocity fields associated pair by pair from one cycle to its following one. The two resulting maps of $C(x, y, T)$ are presented in Fig. 12. A drastic change can be observed depending on the curvature of the front edge. The separation bubble is found to be a strongly uncorrelated region for the high curvature case $\eta = 0.4$ (in the core of the bubble, $C \approx 0.4$ while near the reattachment, $C \approx 0.25$), contrary to the low curvature case $\eta = 0.8$ where the separation bubble remains a highly correlated zone ($C > 0.8$ everywhere inside the bubble). Hence, contrary to the conclusions issued from the tests in previous section, the two flows obtained at $\eta = 0.8$ and $\eta = 0.4$ differ strongly in terms of receptivity with respect to inflow perturbations, the present receptivity being considered through a coefficient that reflects the deterministic conditioning of the flow instabilities by the inlet conditions. Based on this criterion, the strong uncorrelation

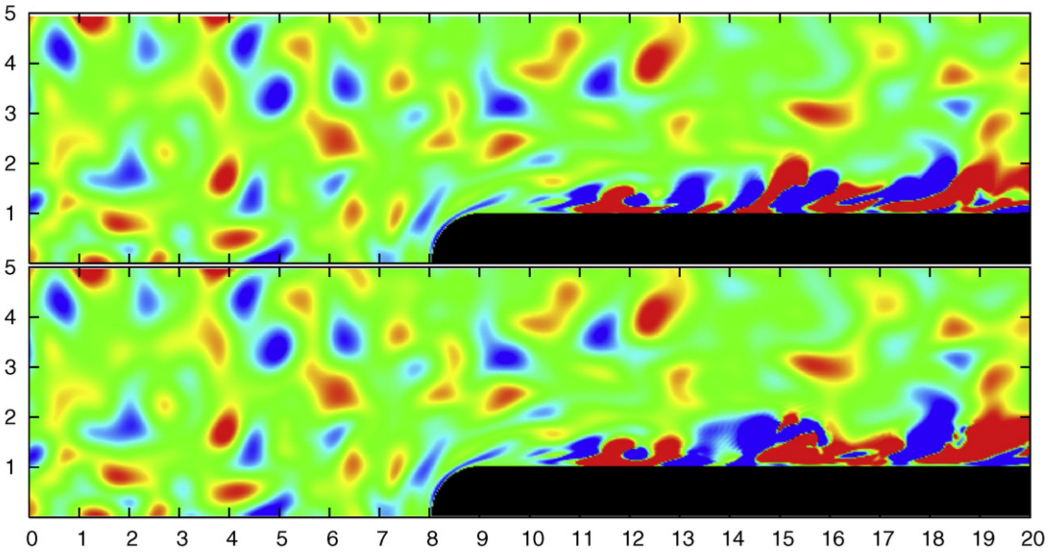

Fig. 10. Example for $\eta = 0.8$ and $\Lambda = \infty$ ($u'_{\mathrm{inflow}} \approx 1\%U_\infty$) of maps of velocity fluctuations (spanwise component w' is obtained here at $z = 0$) for two consecutive cycles of inflow conditions t (top) and $t + T$ (bottom).

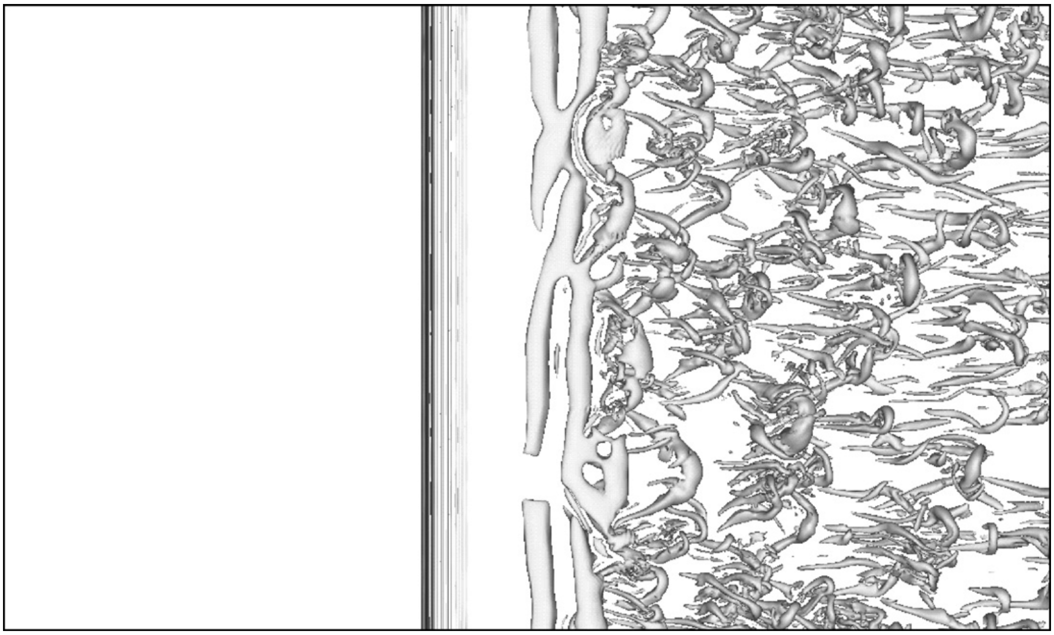

Fig. 11. Top view of the isosurface $Q = 0.25U_\infty^2/H_s^2$ for $\eta = 0.8$ and $\Lambda = \infty$ (initial state corresponding to the final state presented in Fig. 6).

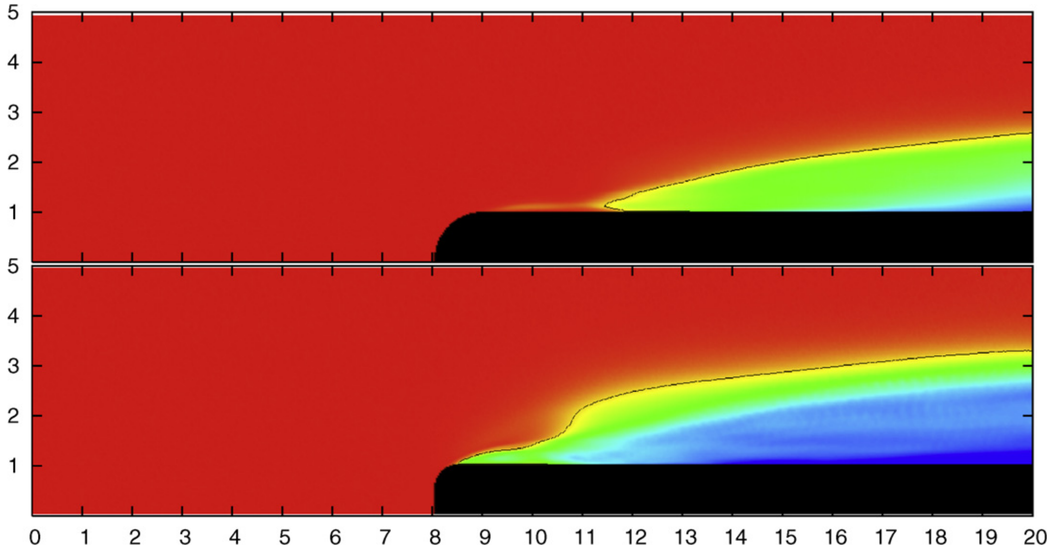

Fig. 12. Maps of $C(x,y,T)$ for $\Lambda = \infty$ and $\eta = 0.8$ (top) or $\eta = 0.4$ (bottom). High values ($C \approx 1$) are in red while low values ($C \approx 0$) are in blue. The black line corresponds to isocontour $C = 0.8$. (For interpretation of the references in colour in this figure legend, the reader is referred to the web version of this article.)

observed inside the bubble for the small front edge radius $\eta = 0.4$ could be interpreted as the signature of trend toward absolute instability, contrary to the case $\eta = 0.8$ that exhibits again the behaviour of a convectively unstable flow.

7. Discussion

In many applications, especially in the car industry, it would be interesting to better control the separated regions of the flow. Consequently, the receptivity of the separation bubble with respect to external conditions needs to be better understood. First, it seems necessary to define more clearly the fundamental characteristics that can be relevantly interpreted. The present study illustrates very well the ambiguities that terms like convectively or absolutely unstable can lead to. In fact, in the context of stability theory, these concepts are rigorously defined, but their link with the behaviour of a given flow needs to be clarified. For instance, without performing a formal stability analysis of the present flows, many numerical observations (especially the tests about the importance of inlet excitation levels) suggest that the 2D body cases $\Lambda = \infty$ exhibit characteristics of convective instability for the two curvatures $\eta = 0.8, 0.4$. However, by analysing here these two flows in a more deterministic way, through comparative visualizations or statistics between analogous flow realizations (here, the analogy was linked to the use of a cyclic inflow condition, but other types of conditioning can be proposed), the two curvature cases appear to be of very different nature in terms of upstream/downstream influence. The temptation to connect this type of influence with the notion of convective/absolute instability is strong, but in this work, this link remains to be clarified.

In their DNS of the flow over a 2D airfoil, Jones et al. (2007) are also submitted to similar ambiguities. For their application, a local stability analysis leads these authors to conclude that the flow is convectively unstable, but in practice, they find that the separation bubble simulated is self-sustaining so that downstream influence seems to be crucial in the breakdown to turbulence of the separated flow. To understand the reason of this self-excitation mechanism, Jones et al. (2007) propose an original use of a DNS code in order to compute the time evolution of a cloud of perturbations initially introduced. The analysis of the behaviour of this type of perturbations (that differs from highly localised perturbations usually used in approaches based on wave packet analysis) allows Jones et al. (2007) to exhibit the global process leading to the self-excitation of perturbations in a separation bubble. However, as in the stability theory, this procedure needs to define a base flow, this definition being able to introduce a bias in the analysis.

To understand the fundamental reasons of the self-excitation of a separation bubble over a 2D wing, Shan et al. (2005) have analysed by DNS the triggering of instabilities in the lack of any inflow disturbances. Through the observation of time histories of pressure fluctuations at different locations along the airfoil chord, they propose a mechanism where the first instabilities start behind the trailing edge (in the wake region), the resulting disturbances being propagated as acoustic waves toward the separation bubble and finally amplified by the unstable separated shear layer. This process of acoustic upstream propagation of disturbances is proposed to explain 3D as well as 2D instabilities in the separation bubble. As this interpretation is based on backward effects through acoustic waves generated from the trailing edge of the airfoil, it cannot be used for the present incompressible flow configuration where the body is semi-infinite (no trailing edge wake). More fundamentally, the analysis of the origin of the instability proposed by Shan et al. (2005) is not necessary connected to the main processes associated with the self-excitation of the bubble in fully non-linear regime.

In present work, compared with the observations of Jones et al. (2007), the situation is almost reversed. Using the criterion based on the intensity of the back flow inside the bubble proposed by Alam and Sandham (2000) (with the critical value of $U_{\min} = -0.15U_{\max}$ for a separated flow over a flat plate), for $\Lambda = \infty$ the high curvature cases $\eta = 0.4$ should be absolutely unstable. It would be due to the strong reverse flow that leads to $U_{\min} = -0.21U_{\max}$. This crude analysis (the critical value of -0.15 corresponds to a specific shape of velocity profile that differs significantly from the ones observed in present study) is contradicted by the behaviour of the bubble when the level of inlet excitation is modified (with no presence of self-excited processes for the case without inflow perturbation), but is consistent with the non-deterministic influence of the inlet excitation itself. To better establish the link between these various concepts, it seems necessary to explore in more detail the present flows by extending the receptivity analysis to the 3D body cases, this next step being significantly more computationally expensive for statistical convergence reasons.

8. Conclusion

The preliminary goal of present study was to reproduce numerically a set of experiments well referenced and calibrated to better understand the formation of a typical separation bubble just behind the rounded edge of a half-body with a finite spanwise length. By easily modelling the body with the IBM, DNS has been performed in a computational configuration as close as possible to the experimental one. The overall agreement found between numerical and experimental results has allowed us to investigate relevantly the mean and instantaneous flows analysed in topological terms as well as through the observation of the vortex dynamics.

The bubble topology is found to be consistent with experiments, its footprint on the surface flow over the top of the body showing a similar organization with a set of six singular points for the case with the smallest aspect ratio. The identification of ejections and bursting for small aspect ratios, and their relationships with the flapping of the separation bubble, is an example of the interest to provide DNS results in complement to the experiments. Another advantage is the easy control of the boundary conditions, which are exactly known, especially the inlet excitation that can be precisely prescribed. This characteristic makes DNS a very attractive tool to study the receptivity of a given flow. This advantage has been exploited here to propose a simple criterion based on the computation of correlations between flow realizations to identify the deterministic regions with respect to inflow disturbances. Due to its simplicity and compatibility with fully non-linear regimes, this criterion seems to be an interesting tool offering an alternative analysis in complement with more formal predictions from stability theory through the concept of convective/absolute behaviour. For the present flow configuration, this type of receptivity analysis exhibits clearly the drastic change of inflow sensitivity of the bubble dynamics depending on the curvature of the leading-edge for a 2D body. More investigation is required to evaluate the interest of this new criterion for a 3D body with a finite width.

As a direct perspective, in order to distinguish more clearly the curvature effects while taking the side bubbles into account, this study should be carried out on a more regular geometry than the present half-bodies that mix sharp and rounded edges so that lateral and top separations (that probably interact) can be of different nature in terms of inflow receptivity. This will be the subject of a further work where the versatility of IBM can be again exploited to consider easily more complex 3D half-bodies shaped to have similar curvature for all their edges.

Acknowledgements

The simulations were carried out at the IDRIS, the computational centre of the CNRS. The authors are grateful to A. Spohn, S. Courtine, E.B. Camano Schettini and J.-P. Bonnet for fruitful discussions and comments on this work.

References

Alam, M., Sandham, N.D., 2000. Direct numerical simulation of short laminar bubbles with turbulent reattachment. J. Fluid Mech. 403, 223–250.

Chomaz, J.-M., 2005. Global instabilities in spatially developing flows: non-normality and nonlinearity. Ann. Rev. Fluid Mech. 37, 357–392.

Courtine, S., 2006. Etude expérimentale des décollements provoqués par une paroi courbe: Topologie et évolution spatio-temporelle. Ph.D. Thesis, Université de Poitiers.

Courtine, S., Spohn, A., 2004. Dynamics of separation bubbles formed on rounded edges. In: 12th International Symposium on Applications of Laser Techniques to Fluid Mechanics. Lisbon, Portugal.

Courtine, S., Spohn, A., Bonnet, J.-P., 2007. Vortex dynamics in the reattaching flow of separation bubbles with variable aspect ratio. In: Proc. 11th European Turbulence Conference, EUROMECH. Porto, Portugal.

Delery, J.-M., 2001. Robert Legendre and Henri Werlé: toward the elucidation of three-dimensional separation. Ann. Rev. Fluid Mech. 33, 129–154.

Huerre, P., Monkewitz, P.A., 1990. Local and global instabilities in spatially developing flows. Ann. Rev. Fluid Mech. 22, 473–537.

Jones, L.E., Sanberg, R.D., Sandham, N.D., 2007. Direct numerical simulation of a laminar separation bubble on a NACA-0012 airfoil. In: Friedrich, R., Adams, N.A., Eaton, J.K., Humphery, J.A.C., Kasagi, N., Leschziner, M.A., Proceedings of the Fifth International Symposium on Turbulence and Shear Flow Phenomena, TU, München, Garching, Germany, 27–29 August 2007, vol. 2, pp. 949–954.

Laizet, S., 2004. Développement d'un code de calcul combinant des schémas de haute précision avec une méthode de frontière immergée pour la simulation des mouvements tourbillonnaires en aval d'un bord de fuite. Ph.D. Thesis, Université de Poitiers.

Laizet, S., Lamballais, E., 2005. Direct numerical simulation of a spatially evolving flow from an asymmetric wake to a mixing layer. In: 6th ERCOFTAC Workshop on Direct and Large-Eddy Simulation. Poitiers, France.

Laizet, S., Lamballais, E., 2006. Simulation numérique directe de l'influence de la forme aval d'une plaque séparatrice sur une couche de mélange. C.R. Mecanique 334, 454–460.

Laizet, S., Lamballais, E., submitted for publication. High-order compact schemes for incompressible flows: a simple and efficient method with the quasi-spectral accuracy. J. Comput. Phys.

Laizet, S., Lardeau, S., Lamballais, E., 2007. Wake effects on streamwise evolution of planar mixing layer. J. Fluid Mech., 1–10 (In revision).

Lesieur, M., Métais, O., Comte, P., 2005. Large-eddy Simulation of Turbulence. Cambridge University Press.

Parnaudeau, P., Lamballais, E., Heitz, D., Silvestrini, J.H., 2003. Combination of the immersed boundary method with compact schemes for DNS of flows in complex geometry. In: Proc. DLES-5. Munich.

Perry, A.E., Chong, M.S., 1986. A series-expansion study of the Navier–Stokes equations with applications to thee-dimensional separation patterns. J. Fluid Mech. 173, 207–223.

Shan, H., Jiang, L., Liu, C., 2005. Direct numerical simulation of flow separation around a NACA 0012 airfoil. Comput. Fluids 34, 1096–1114.

Tobak, M., Peak, D.J., 1982. Topology of three-dimensional separated flows. Ann. Rev. Fluid Mech. 14, 61–85.

Yang, Z., Voke, P., 2001. Large-eddy simulation of boundary-layer separation and transition at a change of surface curvature. J. Fluid Mech. 439, 305–333.